Electric Field Controlled Heat Transfer Through Silicon and Nano-confined Water

Onur Yenigun & Murat Barisik

Taylor & Francis
Taylor & Francis Group

Check for updates

Electric Field Controlled Heat Transfer Through Silicon and Nano-confined Water

Onur Yenigun and Murat Barisik ⓘ

Department of Mechanical Engineering, Izmir Institute of Technology, Izmir, Turkey

ABSTRACT
Nanoscale heat transfer between two parallel silicon slabs filled with deionized water was studied under varying electric field in heat transfer direction. Two oppositely charged electrodes were embedded into the silicon walls to create a uniform electric field perpendicular to the surface, similar to electrowetting-on-dielectric technologies. Through the electrostatic interactions, (i) surface charge altered the silicon/water interface energy and (ii) electric field created orientation polarization of water by aligning dipoles to the direction of the electric field. We found that the first mechanism can manipulate the interface thermal resistance and the later can change the thermal conductivity of water. By increasing electric field, Kapitza length substantially decreased to 1/5 of its original value due to enhanced water layering, but also the water thermal conductivity lessened slightly since water dynamics were restricted; in this range of electric field, heat transfer was doubled. With a further increase of the electric field, electro-freezing (EF) developed as the aligned water dipoles formed a crystalline structure. During EF (0.53 V/nm), water thermal conductivity increased to 1.5 times of its thermodynamic value while Kapitza did not change; but once the EF is formed, both Kapitza and conductivity remained constant with increasing electric field. Overall, the heat transfer rate increased 2.25 times at 0.53 V/nm after which it remains constant with further increase of the electric field.

Introduction

Heat transfer control is crucial in the thermal management applications keeping the working temperatures at a desired condition. Specific for micro/nano-technologies, thermal management is challenging due to the extremely high heat fluxes required and complications developing in heat transfer mechanisms at nanoscales. For this reason, heat transfer control has become one of the main obstacles for further technological developments. Consequently, innovative techniques such as smart materials/systems were developed to control heat transfer at micro/nanoscales. For example, steering heat transfer toward heat sinks using nano-engineered materials [1], designing thermal conductivities by tailoring nanostructures [2, 3], and controlling convection using specialized surfaces [4, 5] are examples of passive control techniques. However, recent technologies require more sophisticated, active control techniques for need-based heat transfer.

One of the major active heat transfer control techniques emerged from the use of an electric field to manipulate the solid and/or liquid domains, and their interface couplings. For example, the major challenge of boiling heat transfer known as the Leidenfrost phenomenon could be resolved by the aid of an electric field [6–8]. The vapor film formed on a surface can be removed

CONTACT Murat Barisik ✉ muratbarisik@iyte.edu.tr 🖾 Department of Mechanical Engineering, Izmir Institute of Technology, Izmir 35430, Turkey

Color versions of one or more of the figures in the article can be found online at www.tandfonline.com/umte.

by drawing liquid toward the surface with an applied electric field to boost surface wetting. Also known as electrowetting, interface energy between solid and liquid can be actively controlled by an electric field [9]. Electrowetting-on-dielectric (EWOD) is its main application where the electrodes are covered by a dielectric layer acting as a capacitor. Variation of wetting angle as a function of the applied electric field was examined theoretically by the Lippmann–Young equation [10, 11]. Fundamentally, an electromechanical force is applied on the system as the Maxwell stress tensor. In the case of an ionic liquid, the prominent net force develops on the ions, which is the conventional EWOD principal. On the other hand, in the case of a deionized polar liquid, a bulk force can only be formed on its dipoles if there is a non-uniform electric field, as described in dielectrowetting applications using dielectrophoretic forces [12]. Instead, a polar dielectric liquid can be controlled by manipulating its molecular dipole distribution in a uniform electric field. For example, dipolar water molecules tend to orient along the applied electric field direction, and such reorientations and shifts produce a net stretching action [13–16]. Orientation polarization in water dominates the intermolecular forces as a function of the electric field strength that water elongates in the direction of the electric field known as electrostretching [15]. Alteration of dipole distribution results in a change of phase transitions of water [17]. Water molecules start to form crystalline structures, even at room temperature, under an electric field, which is known as electro-freezing [18–20]. The ice-like structures were imaged at room temperature by means of atomic force microscopy [21, 22]. Such structural manipulations were proven to be useful for active thermal conductivity control of both solids [23, 24] and liquids [25].

In addition to fundamental convective and conductive heat transfer mechanism, resistance to thermal flow at the interface of dissimilar materials is a determining mechanism for the heat transfer at micro and nanoscales. Interface thermal resistance (ITR) develops due to the phonon mismatch, and it is frequently characterized by the Kapitza length [26, 27]. ITR is the most dominant heat transfer mechanism at nanoscale due to the increase of surface-to-volume ratio. There are multiple experimental, theoretical, and computational studies regarding the dependence of ITR and the resulted heat transfer on interface properties, such as surface wetting [28–30], surface temperature [31, 32], surface atomic density [33], and liquid pressure [34]. Overall, manipulation of surface wetting was conceived as the most effective way to control ITR. Multiple studies were dedicated to characterizing the effect of various forms of surface modifications, such as surface patterning [35, 36], surface conditions [37], coating material [38–40], and thickness of solid coating [41], which provide a passive ITR control. Instead, coupling at the liquid–solid interface can be actively controlled using an electric field. In our earlier studies, we implemented such an idea for manipulation of the momentum coupling (velocity slip) at water/graphene interface and achieved control of the mass flow rate [42–43]. To the best of our knowledge, ITR control via electric field has never been investigated in the literature.

In this study, we are investigating a smart thermal management concept, where the heat transfer rate can be controlled actively by changing the electric field applied onto the micro/nano-fluidic system. Electric field affects both water hydrodynamics and its coupling with the silicon surface. Water thermal conductivity, water density layering, and ITR will be studied as a function of electric field strength.

Simulation details

Water confined between two silicon slabs was simulated as illustrated in Figure 1. Cross-sectional area of the computational domain was 3.8 × 3.8 nm in the surface parallel directions where periodic boundary conditions were applied. The distance between 5.4 nm thick silicon slabs was 5.7 nm and (0,0,1) crystal plane was facing the fluid. Non-equilibrium molecular dynamics (NEMD) simulations were performed with LAMMPS (Large-scale Atomic/Molecular Massively Parallel Simulator) algorithm.
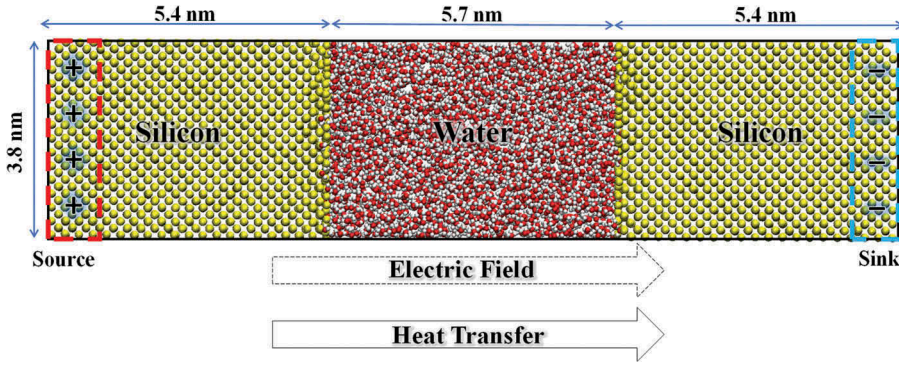
Figure 1. Simulation domain.

SPC/E water model composed of Lennard-Jones and Coulombic potentials is used with SHAKE algorithm to constrain the bond lengths and angles of this rigid model. Stillinger–Weber potential is used for the Si–Si interactions, which considers two-body interactions with an additional many body dependence [44]. Interactions between water and silicon also calculated by the combined Lennard-Jones and Coulombic potentials. Parameters for the interactions between similar molecules such as O–O and Si–Si were taken from the corresponding models. However, the parameters determining the interactions of the specific liquid/solid couples are still under investigation. Frequently, interaction parameters for dissimilar molecules are calculated using simple mixing rules as a function of parameters of the pair of identical molecules. However, the interaction parameters between identical molecules are optimized for a bulk material system that parameters calculated based on a mixing rule cannot recover the correct behavior at the given solid/liquid interface. In our earlier wetting study based on MD, measured contact angles of water nano-droplets showed that experimentally measured hydrophobic behavior of silicon surfaces can be recovered when the silicon–oxygen interaction strength is 12.5% of the value predicted using the Lorentz–Berthelot mixing rule [45]. Hence, we employed this interaction strength value in the current study. The molecular interaction parameters for each molecule pair used in the simulations are given in Table 1.

Atoms in the outmost layer of both silicon slabs are fixed to their original locations to maintain a fixed volume system, while the remaining atoms throughout the domain were free to move. The fixed outmost silicon layers were selected as electrodes to apply equally distributed charge per molecule. Negative and positive charges with equal absolute value were assigned at the electrodes of the right and left side. A uniform electric field develops in the surface normal direction. Applied surface charge densities were varied between 0.05 and 0.6 C/m^2, which resulted in electric fields strengths varying between 0.09 and 0.96 V/nm, similar to earlier MD studies [15, 16, 20, 42]. Although applied electric fields seem high for experimental studies, it is not totally impractical [18]. For example, the pulse discharge method engages pulse voltages through two electrodes in an aqueous environment to generate an electric field on the order of 1 V/nm [18, 46, 47] similar to studied electric field strengths.

The particle–particle particle-mesh solver was used to calculate long-range Coulombic interactions of the periodic slab system. By using the Verlet algorithm with a time step of 0.001 ps, Newton's equations of motion were integrated. Simulations were started from the Maxwell–

Table 1. Molecular interaction parameters used in the current study.

Molecule pair	σ (Å)	ε (eV)	q (e)
O–O	3.166	0.006739	−0.8476
H–H	0	0	+0.4238
Si–Si	2.095	2.168201	0
Si–O	2.6305	0.01511	Varies

Boltzmann velocity distribution for all molecules at 323 K, while NVT (constant number of molecules, constant volume and constant temperature) ensemble was applied with Nose Hover thermostat keeping the system at 323 K. To reach an isothermal steady state, initial particle distribution was evolved 2×10^6 time-steps (2 ns). Afterward, one-dimensional heat transfer between silicon slabs was created using the Nose Hover thermostat applied only to the outmost six layers of the both silicon slabs. Left and right side thermostats were maintained at 363 and 283 K temperatures to induce heat flux through the liquid/solid interfaces. Such high-temperature gradients can be developed by using the electron beam of a transmission electron microscope or the plasmonic nanoantenna, similar to thermophoresis [48] or heat-assisted magnetic recording [49, 50] applications. At the same time, NVE (constant number of molecules, constant volume and constant energy) ensemble was applied to the remaining silicon and water molecules. Simulations were performed for an additional 15×10^6 time-steps (15 ns) to ensure that the system attains equilibrium in the presence of the heat flux and time averaging is performed after the equilibrium is achieved. The computational domain was divided into 124 slab bins with the size of 0.1343 nm for temperature profiles. Smaller bin size, 1476 slab bins with the size of 0.0113 nm, was also employed to resolve the fine details of the near-wall water density distributions.

Results

A positive uniform surface charge density was applied on the left electrode section as the anode while an equal but negative uniform surface charge density was applied on the right electrode representing the cathode. Hence, a uniform electric field was created in the system pointing from left to right. In Figure 2, resulting temperature distributions at different electric field strengths of 0, 0.18, 0.35, and 0.79 V/nm were plotted. The temperature profiles show variation by the applied electric field. Temperature profiles are linear in the water domain except the very near-wall regions, where temperature profile fluctuates due to the density layering created by the Van der Waals force field of surface and the electric field. When the electric field strength reaches to 0.79 V/nm, temperature profile starts to fluctuate through the whole channel. Such behavior is expected, since the corresponding amplitude of the electric field is enough to cause electro- freezing [15, 16, 20, 42]. When electro-freezing occurs, water molecules start forming an ordered structure. Due to these ordered structures, number of molecules fluctuate for the case of current fine binning through the domain. Instead, if a coarser binning was applied as an average of every four bins, for instance, a linear temperature profile would be obtained. This means that, Fourier's Law of heat conduction is still applicable in highly ordered water system under the effect of an electric field. Temperature profiles
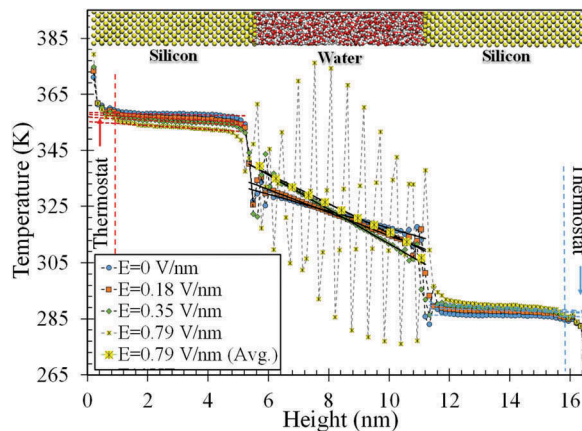

Figure 2. Temperature distributions at electric field strengths of 0, 0.18, 0.35 and 0.79 V/nm.

for the case with electric field strength of 0.79 V/nm, by both fine and coarse binning are given in Figure 2 using similar markers with different sizes. Furthermore, there is a jump between silicon and water temperatures at the interface due to the phonon mismatch. This is the well-known interfacial thermal resistance.

Next, we studied the density distributions of water under different electric field strengths. We presented the results of the studied electric fields range of 0–0.96 V/nm in two groups as low and high electric fields. The high field denotes the range through which electro-freezing develops. In Figure 3, water density distributions at low electric field range varying between 0 and 0.40 V/nm were given. The well-known density layering extending a couple of molecular diameter length from the surfaces develops while density reaches its thermodynamic value of 1 g/cm^3 at the rest of the channel. Two distinct density peaks are observed while a third one at very near surface develops at high electric fields. Near-wall density layers are pulled toward the surface by increasing electric field. Water penetrates under the first silicon layer in the zero-charge case similar to earlier studies [31, 45]. The increase of electric field develops further water penetration into the silicon surface. This can be also denoted as a change of surface energy or surface wetting. By the increasing surface charges (i.e. increasing electric field strength), the number of molecules near-wall regions increases, which enhances the interfacial energy of the initially hydrophobic silicon surface.

Details of water density were studied with a higher resolution near both hot and cold surfaces in Figure 4. In a closer view, it is observed that the water penetration into silicon is negligible at zero-electric field case due to the hydrophobic behavior of the silicon surface as documented in the silicon wetting study of Barisik and Beskok [45]. However, with increasing electric field strength, water molecules penetrate into and further under the first silicon layer. At the electric field strength values of 0.35 and 0.4 V/nm, water fills the molecular gaps of the second silicon layer. The nearest density peak and penetration increases by the increase of electric field strength. By the formation of the
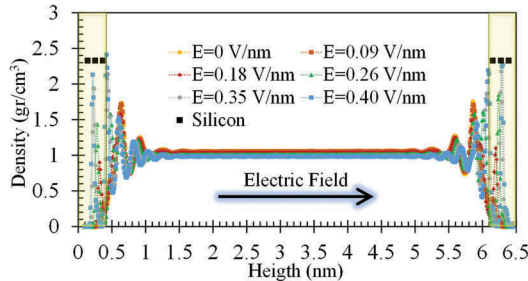

Figure 3. Water density distributions at low electric field range.
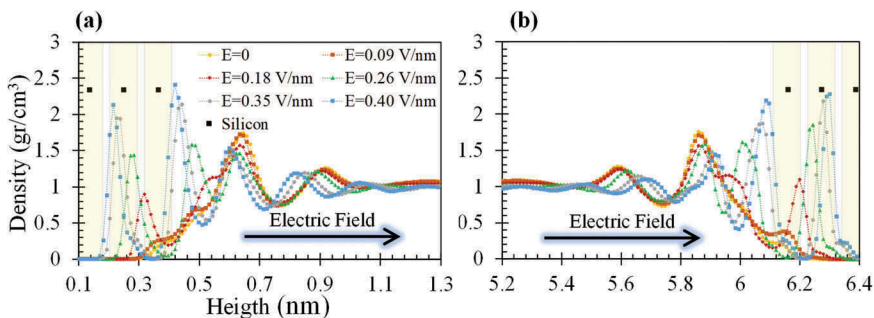

Figure 4. Water density distributions at low electric field range (a) near hot surface with positively charged electrode and (b) near cold surface with negatively charged electrode.

nearest third density peak for electric field values higher than 0.26 V/nm, other two density peaks decrease, and move slightly toward the surface. The water profiles near left and right surfaces are identical at zero-charge case, even though the surface temperatures are different. Density layering was found independent of surface temperature for hydrophobic surfaces in our earlier study [31]. However, under electric field, water dipoles tend to line up with the electric field direction that oxygen molecules try to face positive electrode while hydrogen molecules turn toward negative electrode. Hence, non-symmetrical distribution develops by increasing electric field. This is called polarity bias which particularly observed at nano-droplets as a variation of contact angle in the electric field direction when it is parallel to surface.

Density distributions of water under high electric field range of 0.44–0.96 V/nm are given in Figure 5. The first sign of electro-freezing was observed at 0.44 V/nm on the right side of the water domain. Temperature profile of 0.44 V/nm case shows that water temperature changes from 330 to 310 K from left side to right side. We know that electric field shifts the phase transition of water [15, 16, 20, 42]. Since the water at temperatures higher than 325 K remains as a liquid, we can simply state that 0.44 V/nm results in the change of freezing temperature to approximately 325 K. Electric fields higher than 0.44 V/nm results in complete freezing of water that the whole water domain gets in solid like ordering. The closer view of the near-wall water density distributions at high electric field range are given in Figure 6. Water density ordering is in transitions at 0.44 V/nm, but water structure remains unchanged for higher field strengths.

The molecular orientations of water at different electric field strengths are presented in Figure 7. As described through the density distributions, water molecules first get attracted to the dielectric silicon surfaces and penetrate in and under the first silicon layer. First crystal ordering develops at 0.44 V/nm
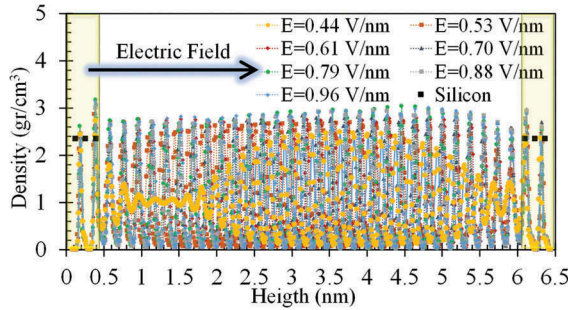

Figure 5. Density distributions of water at high electric field range varying from 0.44 to 0.96 V/nm.
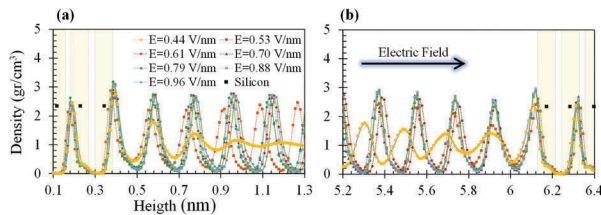

Figure 6. Water density distributions of high electric field range (a) near hot surface with positively charged electrode and (b) near cold surface with negatively charged electrode.
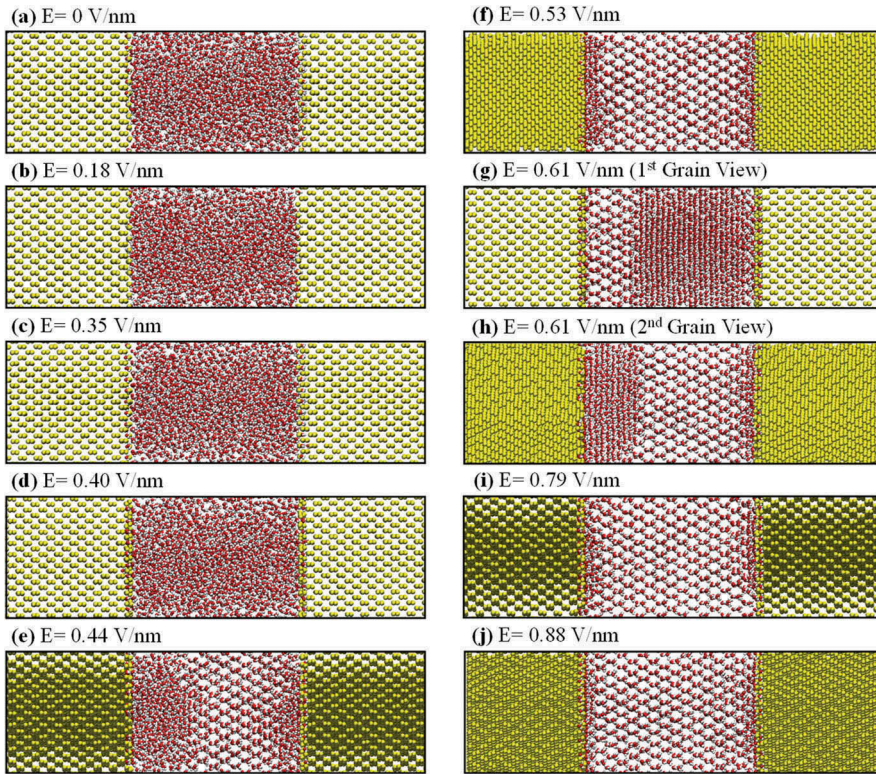
Figure 7. The snapshots of the silicon/water system at electric fields of (a) 0, (b) 0.18, (c) 0.35, (d) 0.40, (e) 0.44, (f) 0.53, (g) 0.61, (h) 0.61, (i) 0.79, and (j) 0.88 V/nm.

that we can observe the water molecules at a hexagonal structure near to the cold side of domain (Figure 7e). By increasing the electric field further, the complete crystallization develops. Such crystalline structure formation is a result of electric field-induced change in hydrogen bond network [42]. At strong electric field, random molecular motions and hydrogen bond dynamics become restricted into electric field direction that water forms a crystalline structure. These structures developed in the single crystalline form, except the case at electric field strength of 0.61 V/nm which created two grains with different crystal ordering. In order to observe the crystal structures, we rotated the systems to have best snapshot in Figure 7. Single crystalline structures can be easily seen in Figure 7f, i and j while the view of both grains developed at 0.61 V/nm is given in Figure 7g,h.

A detailed characterization of the crystalline structure is studied in Figure 8. Different views of the silicon/water domain at 0.88 V/nm are presented. Just simple three-dimensional and side view given in Figure 8a,b presents the highly ordered water molecules. When the system is viewed at different angles, a perfect (0,0,1) and (1,0,1) crystallographic ice planes can be observed in Figure 8c,d, respectively. This can validate the perfect crystalline structure as the results agree with the electro-freezing study of Yan and Patey [20].

Next, we studied the water temperature profiles normalized with their average values under low and high electric field strengths in Figure 9a,b, respectively. At low field range prior to electro-structuring, temperature profiles vary by applied electric field. Basically, the slopes of the temperature profiles are increasing with the increasing electric field while the temperature difference between hot and cold reservoirs is kept constant. On the other hand, at the same temperature difference, temperature gradient of high electric fields cases remained unchanged by the increase of field strength. For comparison reasons, we added low electric field case of 0.4 V/nm (no freezing) in
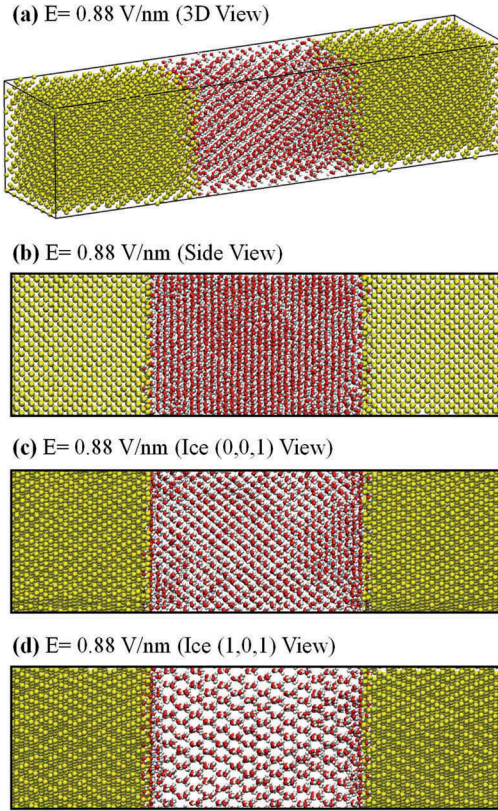
(a) E= 0.88 V/nm (3D View)

(b) E= 0.88 V/nm (Side View)

(c) E= 0.88 V/nm (Ice (0,0,1) View)

(d) E= 0.88 V/nm (Ice (1,0,1) View)

Figure 8. The snapshots of the silicon/water system under 0.88 V/nm electric field at (a) 3D view, (b) side view, (c) ice (0,0,1) view, and (d) ice (1,0,1) view.
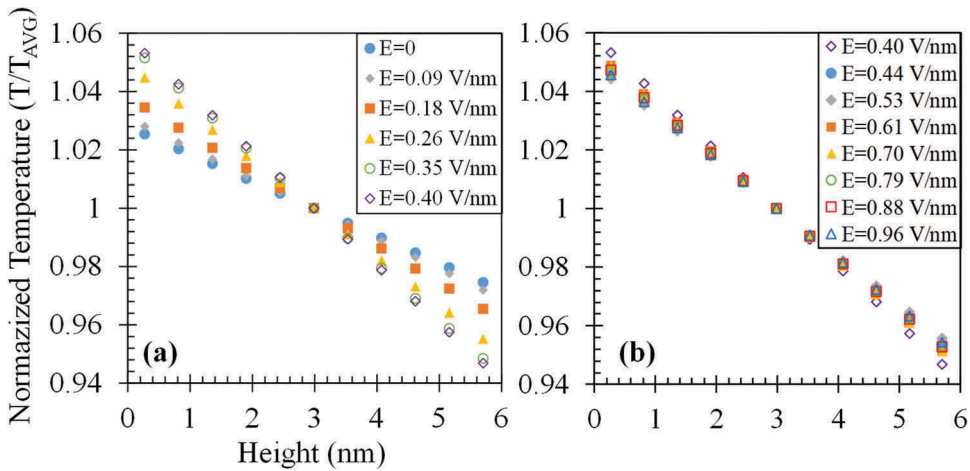
Figure 9. Normalized temperature profiles of water under electric fields varying from (a) 0 to 0.4 V/nm and (b) 0.4 to 0.96 V/nm.

Figure 9b. After the electro-freezing developed at 0.44 V/nm case, temperature profiles of different electric fields are almost identical.

Observed change of temperature gradients at a constant temperature difference is due to the change in the heat flux. In the current system, heat transfer is determined by the thermal resistances to (i) heat transfer by conduction and (ii) heat transfer through interfaces. In the next sections, we studied the variations in the thermal conductivity of water and ITR at different electric field strengths.

First, water thermal conductivities calculated from the measured heat fluxes and temperature gradients. Since the temperature profiles of water are linear (Figure 9), we used Fourier's Law of heat conduction as $k = q/(\partial T/\partial z)|_{liquid}$ to calculate conductivities of water, where (q) is the heat flux and ($\partial T/\partial z$) is the temperature gradient. Results are presented in Figure 10a. For the zero-electric field case, thermal conductivity was calculated as 0.82 W/mK at the average temperature of 325 K, which agrees with the literature [51]. With increasing electric field, thermal conductivity of water slightly decreases with the increase of electric field strength in the low electric field range (<0.44 V/nm). This is due to the restricted molecular diffusion and hydrogen bonding activities of water molecules under electric field. After reaching electric field strength of 0.44 V/nm, water thermal conductivity shows a sudden jump due to the formation of crystalline structure. Thermal conductivity of water increases 1.5 times when electric field strength reaches to 0.53 V/nm and then remains constant with the increased electric field. There is just one exception that thermal conductivity decreases some at 0.61 V/nm. Interestingly, at electric field strength of 0.61 V/nm, the perfect crystalline structure is disturbed when the water molecules form two crystalline grains. Formation of grain boundaries interrupts the heat transfer that the thermal conductivity is reduced at this electric field.

Next, ITRs were characterized by calculating Kapitza lengths. Based on the temperature jump at the liquid/solid interface (ΔT) and the temperature gradient of the liquid ($\partial T/\partial z$), Kapitza length (L_K) was calculated using $L_K = \Delta T/(\partial T/\partial z)|_{liquid}$. Results are given in Figure 10b for both hot and cold surfaces. Kapitza length shows a drastic decrease by the application of electric field. In the low electric field range, L_K reduces to 1/5 of its original value. This can be attributed to enhanced surface wetting decreasing the ITR. Solid/liquid coupling improves by the increased water density near surface as a function of electric field. Minimum ITR develops approximately at 0.40 V/nm right before the electro-freezing starts. While the L_K on hot surface is lower than the L_K on cold side at the zero-electric field case, L_K on hot side becomes higher than the cold side value through the low electric field range. Temperature dependence of L_K at liquid/solid interface described in detail in our earlier study [31]. Simply, variation of L_K by temperature is determined by the temperature dependence of phonon dynamics on hydrophobic surfaces, while it is dominated by the temperature dependence of near-surface liquid layering on hydrophilic surfaces. For such a case, electric field shifts the surface wetting from hydrophobic to hydrophilic and water domain still acts as a liquid at
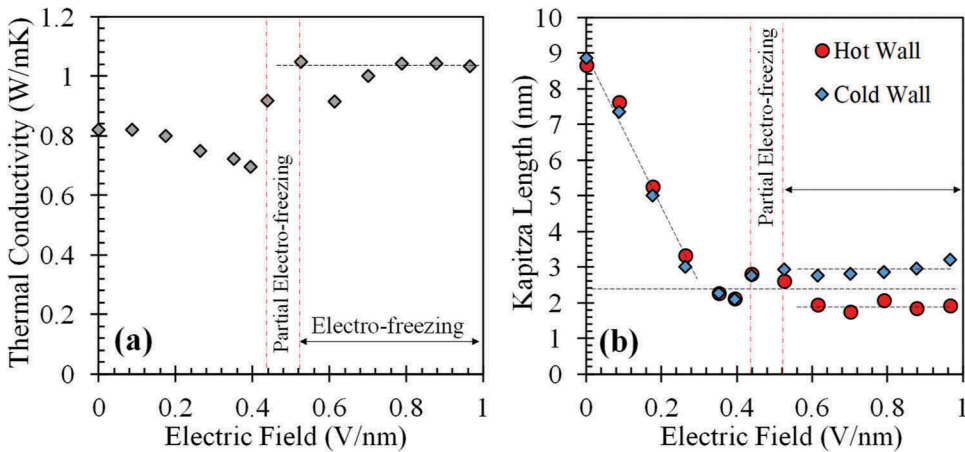

Figure 10. (a) Thermal conductivity of water and (b) Kapitza length as a function of electric field strength.
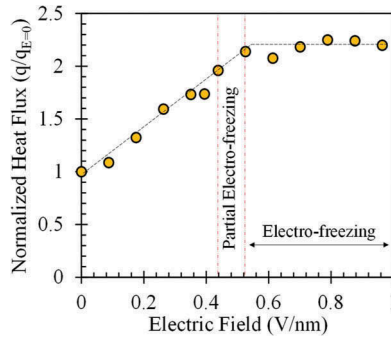
Figure 11. Normalized heat flux through the nano-confined water as a function of applied electric field strength.

low electric field range without freezing. Once the water molecules form crystalline structure, the ITR slightly increases. This is due to decreased coupling by the shrink of liquid system at the crystalline form. At high electric field range, L_K values on hot surface are lower than L_K on cold surface and their difference slightly increases by the increasing electric field. This behavior is agreeing with enhanced phonon activities at higher temperatures described by classical phonon dynamics theories of solids. After electro-freezing, water system acts as a solid and water structure closer at higher temperature excites and vibrates more lowering the phonon mismatch. The average of L_K at hot and cold side remains constant by the increase of electric field in this high field range. Furthermore, grain formation was found affecting only the water thermal conductivity, not the interfacial thermal resistance. We also measured thermal conductivities of silicon slabs at different electric field, which remained constant at around 9 W/mK, independent of the applied electric field.

The heat flux values for both low and high electric filed ranges are normalized with the heat flux value of the zero-electric field case and given in Figure 11. The heat flux changes with the variation in water thermal conductivity and interfacial thermal resistance by the applied electric field. In the low electric field region ($0 < E < 0.40$ V/nm), the heat flux increases with the increasing electric field strength, which agrees well with the increase in the slope of the water temperature profiles. Even though the thermal conductivity of water decreases slightly in the low electric field region, the significant decrease in the interfacial thermal resistance doubles the heat flux compared to the zero-electric field case. In the case of further increase of the electric field, first, heat flux continues increasing during the crystal formation. Water domain is partially crystallized at 0.44 V/nm and turns completely crystalline at 0.53 V/nm, and water thermal conductivity increase through this electro-freezing range. The heat flux reaches 2.25 times of zero-electric field value at 0.53 V/nm. After the complete crystalline structure is formed ($E = 0.53$ V/nm), the heat flux remains constant, as the further increase in electric field strength does not change the thermal conductivity and interfacial thermal resistance.

Conclusion

We introduced and described the manipulation of heat transfer through nanoscale fluidic systems via an applied electric field. The heat flux can be more than doubled by an electric field in the surface normal direction. Observed behavior was described by characterizing electric field effects on heat transfer mechanisms. Fundamentally, a uniform electric field applies electrostatic forces on dipolar water and manipulates its dipole orientation. Hence, surface wetting and molecular distribution of water can be controlled as a function of electric field strength. Simply, increasing the electric field enhances the solid/liquid coupling at the interface and decreases the ITR substantially until electro-freezing occurs, after which it almost remains constant. On the other hand, increasing the electric field restrains the molecular dynamics in the water domain and decreases the thermal conductivity

slightly until the electro-freezing, during which thermal conductivity increases suddenly but once the full formation developed conductivity remains constant. As a result of these two occurrences, heat flux increases with the increase of electric field up to full formation of electro-freezing. At a constant temperature difference, heat transfer rate increased 2.25 times from zero-electric field to 0.53 V/nm field strength.

Acknowledgments

Funding

ORCID

Murat Barisik http://orcid.org/0000-0002-2413-1991

References

[1] K. M. Razeeb, E. Dalton, G. L. W. Cross, and A. J. Robinson, "Present and future thermal interface materials for electronic devices," *Int. Mater.Rev.*, vol. 63, no. 1, pp.1–21, 2018. DOI: 10.1080/09506608.2017.1296605.

[2] B. Li, K. T. Tan, and J. Christensen, "Tailoring the thermal conductivity in nanophononic metamaterials," *Phys. Rev. B*, vol. 95, no. 14, pp.144305, 2017. DOI: 10.1103/PhysRevB.95.144305.

[3] M. Nomura, J. Shiomi, T. Shiga, and R. Anufriev, "Thermal phonon engineering by tailored nanostructures," *Jpn J. Appl. Phys.*, vol. 57, no. 8, pp.080101, 2018. DOI: 10.7567/JJAP.57.080101.

[4] A. R. Motezakker, *et al.*, "Optimum ratio of hydrophobic to hydrophilic areas of biphilic surfaces in thermal fluid systems involving boiling," *Int. J. Heat Mass Transf.*, vol. 135, pp. 164–174, 2019. DOI: 10.1016/j.ijheatmasstransfer.2019.01.139.

[5] A. R. Betz, J. Jenkins, and D. Attinger, "Boiling heat transfer on superhydrophilic, superhydrophobic, and superbiphilic surfaces," *Int. J. Heat Mass Transf.*, vol. 57, no. 2, pp.733–741, 2013. DOI: 10.1016/j.ijheatmasstransfer.2012.10.080.

[6] B. B. Wang, X. D. Wang, T. H. Wang, G. Lu, and W. M. Yan, "Enhancement of boiling heat transfer of thin water film on an electrified solid surface," *Int. J. Heat Mass Transf.*, vol. 109, pp. 410–416, 2017. DOI: 10.1016/j.ijheatmasstransfer.2017.02.029.

[7] A. Shahriari, P. Birbarah, J. Oh, N. Miljkovic, and V. Bahadur, "Electric field–based control and enhancement of boiling and condensation," *Nanoscale Microscale Thermophys. Eng.*, vol. 21, no. 2, pp.102–121, 2017. DOI: 10.1080/15567265.2016.1253630.

[8] A. Sur, Y. Lu, C. Pascente, P. Ruchhoeft, and D. Liu, "Pool boiling heat transfer enhancement with electrowetting," *Int. J. Heat Mass Transf.*, vol. 120, pp. 202–217, 2018. DOI: 10.1016/j.ijheatmasstransfer.2017.12.029.

[9] F. Mugele and J. C. Baret, "Electrowetting: from basics to applications," *J. phys. condens. matter*, vol. 17, no. 28, pp.R705, 2005.

[10] D. Orejon, K. Sefiane, and M. E. Shanahan, "Young-Lippmann equation revisited for nano-suspensions," *Appl. Phys. Lett.*, vol. 102, no. 20, pp.201601, 2013. DOI: 10.1063/1.4807120.

[11] C. D. Daub, D. Bratko, K. Leung, and A. Luzar, "Electrowetting at the nanoscale," *J. Phys. Chem. C*, vol. 111, no. 2, pp.505–509, 2007. DOI: 10.1021/jp067395e.

[12] A. M. J. Edwards, C. V. Brown, M. I. Newton, and G. McHale, "Dielectrowetting: the past, present and future," *Curr. Opin. Colloid Interface Sci.*, vol. 36, pp. 28–36, 2018. DOI: 10.1016/j.cocis.2017.11.005.

[13] F. H. Song, B. Q. Li, and C. Liu, "Molecular dynamics simulation of nanosized water droplet spreading in an electric field," *Langmuir*, vol. 29, no. 13, pp.4266–4274, 2013. DOI: 10.1021/la304763a.

[14] M. W. Lee, S. S. Latthe, A. L. Yarin, and S. S. Yoon, "Dynamic electrowetting-on-dielectric (DEWOD) on unstretched and stretched Teflon," *Langmuir*, vol. 29, no. 25, pp.7758–7767, 2013. DOI: 10.1021/la401669w.

[15] T. H. Yen, "Investigation of the effects of perpendicular electric field and surface morphology on nanoscale droplet using molecular dynamics simulation," *Mol. Simul.*, vol. 38, no. 6, pp.509–517, 2012. DOI: 10.1080/08927022.2011.633257.

[16] W. D. Luedtke, J. Gao, and U. Landman, "Dielectric nanodroplets: structure, stability, thermodynamics, shape transitions and electrocrystallization in applied electric fields," *J. Phys. Chem. C*, vol. 115, no. 42, pp.20343–20358, 2011. DOI: 10.1021/jp206673j.

[17] X. Zhu, Q. Yuan, and Y. P. Zhao, "Phase transitions of a water overlayer on charged graphene: from electromelting to electrofreezing," *Nanoscale*, vol. 6, no. 10, pp.5432–5437, 2014. DOI: 10.1039/c3nr06596k.

[18] S. Wei, X. Xiaobin, Z. Hong, and X. Chuanxiang, "Effects of dipole polarization of water molecules on ice formation under an electrostatic field," *Cryobiology*, vol. 56, no. 1, pp.93–99, 2008. DOI: 10.1016/j.cryobiol.2007.10.173.

[19] R. Zangi and A. E. Mark, "Electrofreezing of confined water," *J. Chem. Phys.*, vol. 120, no. 15, pp.7123–7130, 2004. DOI: 10.1063/1.1687315.

[20] J. Y. Yan and G. N. Patey, "Molecular dynamics simulations of ice nucleation by electric fields," *J. Phys. Chem. A*, vol. 116, no. 26, pp.7057–7064, 2012. DOI: 10.1021/jp3039187.

[21] O. Teschke, "Imaging ice-like structures formed on HOPG at room temperature," *Langmuir*, vol. 26, no. 22, pp.16986–16990, 2010. DOI: 10.1021/la103227j.

[22] K. B. Jinesh and J. W. M. Frenken, "Experimental evidence for ice formation at room temperature," *Phys. Rev. Lett.*, vol. 101, no. 3, pp.036101, 2008. DOI: 10.1103/PhysRevLett.101.036101.

[23] J. F. Ihlefeld, *et al.*, "Room-temperature voltage tunable phonon thermal conductivity via reconfigurable interfaces in ferroelectric thin films," *Nano Lett.*, vol. 15, no. 3, pp.1791–1795, 2015. DOI: 10.1021/nl504505t.

[24] J. A. Seijas-Bellido, H. Aramberri, J. Íñiguez, and R. Rurali, "Electric control of the heat flux through electrophononic effects," *Phys. Rev. B*, vol. 97, no. 18, pp.184306, 2018. DOI: 10.1103/PhysRevB.97.184306.

[25] W. Evans, J. Fish, and P. Keblinski, "Thermal conductivity of ordered molecular water," *J. Chem. Phys.*, vol. 126, no. 15, pp.154504, 2007. DOI: 10.1063/1.2723071.

[26] G. L. Pollack, "Kapitza resistance," *Rev. Mod. Phys.*, vol. 41, no. 1, pp.48, 1969. DOI: 10.1103/RevModPhys.41.48.

[27] J. D. N. Cheeke, "The kapitza resistance and heat transfer at low temperatures," *Le Journal de Physique Colloques*, vol. 31, no. C3, pp.C3–C129, 1970. DOI: 10.1051/jphyscol:1970312.

[28] A. T. Pham, M. Barisik, and B. Kim, "Molecular dynamics simulations of Kapitza length for argon-silicon and water-silicon interfaces," *Int. J. Precision Eng. Manuf.*, vol. 15, no. 2, pp.323–329, 2014. DOI: 10.1007/s12541-014-0341-x.

[29] Z. Ge, D. G. Cahill, and P. V. Braun, "Thermal conductance of hydrophilic and hydrophobic interfaces," *Phys. Rev. Lett.*, vol. 96, no. 18, pp.186101, 2006. DOI: 10.1103/PhysRevLett.96.186101.

[30] Z. Shi, M. Barisik, and A. Beskok, "Molecular dynamics modeling of thermal resistance at argon-graphite and argon-silver interfaces," *Int. J.Ther. Sci.*, vol. 59, pp. 29–37, 2012. DOI: 10.1016/j.ijthermalsci.2012.04.009.

[31] M. Barisik and A. Beskok, "Temperature dependence of thermal resistance at the water/silicon interface," *Int. J. Ther. Sci.*, vol. 77, pp. 47–54, 2014. DOI: 10.1016/j.ijthermalsci.2013.10.012.

[32] M. Barisik and A. Beskok, "Boundary treatment effects on molecular dynamics simulations of interface thermal resistance," *J Comput. Phys.*, vol. 231, no. 23, pp.7881–7892, 2012. DOI: 10.1016/j.jcp.2012.07.026.

[33] T. Q. Vo, M. Barisik, and B. Kim, "Atomic density effects on temperature characteristics and thermal transport at grain boundaries through a proper bin size selection," *J. Chem. Phys.*, vol. 144, no. 19, pp.194707, 2016. DOI: 10.1063/1.4949763.

[34] A. Pham, M. Barisik, and B. Kim, "Pressure dependence of Kapitza resistance at gold/water and silicon/water interfaces," *J. Chem. Phys.*, vol. 139, no. 24, pp.244702, 2013. DOI: 10.1063/1.4851395.

[35] Y. Hong, L. Li, X. C. Zeng, and J. Zhang, "Tuning thermal contact conductance at graphene–copper interface via surface nanoengineering," *Nanoscale*, vol. 7, no. 14, pp.6286–6294, 2015. DOI: 10.1039/c5nr00564g.

[36] Z. Liang, K. Sasikumar, and P. Keblinski, "Thermal transport across a substrate–thin-film interface: effects of film thickness and surface roughness," *Phys. Rev. Lett.*, vol. 113, no. 6, pp.065901, 2014. DOI: 10.1103/PhysRevLett.113.065901.

[37] X. Liu, G. Zhang, and Y. W. Zhang, "Topological defects at the graphene/h-BN interface abnormally enhance its thermal conductance," *Nano Lett.*, vol. 16, pp. 4954–4959, 2016.

[38] A. T. Pham, M. Barisik, and B. Kim, "Interfacial thermal resistance between the graphene-coated copper and liquid water," *Int. J. Heat Mass Transf.*, vol. 97, pp. 422–431, 2016. DOI: 10.1016/j.ijheatmasstransfer.2016.02.040.

[39] J. Zhang, *et al.*, "Molecular dynamics simulation of the interfacial thermal resistance between phosphorene and silicon substrate," *Int. J. Heat Mass Transf.*, vol. 104, pp. 871–877, 2017. DOI: 10.1016/j.ijheatmasstransfer.2016.08.021.

[40] A. Y. Nobakht and S. Shin, "Anisotropic control of thermal transport in graphene/Si heterostructures," *J. Appl. Phys.*, vol. 120, no. 22, pp.225111, 2016. DOI: 10.1063/1.4971873.

[41] O. Yenigun and M. Barisik, "Effect of nano-film thickness on thermal resistanec at water silicon interface," *Int. J. Heat Mass Transf.*, vol. 134, pp. 634–640, 2019. DOI: 10.1016/j.ijheatmasstransfer.2019.01.075.

[42] A. T. Celebi, M. Barisik, and A. Beskok, "Electric field controlled transport of water in graphene nano-channels," *J. Chem. Phys.*, vol. 147, no. 16, pp.164311, 2017. DOI: 10.1063/1.4996210.

[43] A. T. Celebi, M. Barisik, and A. Beskok, "Surface charge-dependent transport of water in graphene nano-channels," *Microfluid. Nanofluid.*, vol. 22, no. 1, pp.7, 2018. DOI: 10.1007/s10404-017-2027-z.

[44] F. H. Stillinger and T. A. Weber, "Computer simulation of local order in condensed phases of silicon," *Phys. Rev. B*, vol. 31, no. 8, pp.5262, 1985. DOI: 10.1103/PhysRevB.31.5262.

[45] M. Barisik and A. Beskok, "Wetting characterisation of silicon (1, 0, 0) surface," *Mol. Simul.*, vol. 39, no. 9, pp.700–709, 2013. DOI: 10.1080/08927022.2012.758854.

[46] I. Braslavsky and S. G. Lipson, "Electrofreezing effect and nucleation of ice crystals in free growth experiments," *Appl. Phys. Lett.*, vol. 72, no. 2, pp.264–266, 1998. DOI: 10.1063/1.120705.

[47] P. Šunka, "Pulse electrical discharges in water and their applications," *Phys. Plasmas.*, vol. 8, no. 5, pp.2587–2594, 2001. DOI: 10.1063/1.1356742.

[48] H. Somada, K. Hirahara, S. Akita, and Y. Nakayama, "A molecular linear motor consisting of carbon nanotubes," *Nano Lett.*, vol. 9, no. 1, pp.62–65, 2008. DOI: 10.1021/nl802323n.

[49] S. Jones, D. Andrén, P. Karpinski, and M. Käll, "Photothermal heating of plasmonic nanoantennas: influence on trapped particle dynamics and colloid distribution," *ACS Photonics*, vol. 5, no. 7, pp.2878–2887, 2018. DOI: 10.1021/acsphotonics.8b00231.

[50] B. Dieny, *et al.*, "Impact of intergrain spin-transfer torques due to huge thermal gradients in heat-assisted magnetic recording," *IEEE Trans. Magn.*, vol. 54, no. 12, pp.1–11, 2018. DOI: 10.1109/TMAG.2018.2863225.

[51] Y. Mao and Y. Zhang, "Thermal conductivity, shear viscosity and specific heat of rigid water models," *Chem. Phys, Lett.*, vol. 542, pp. 37–41, 2012. DOI: 10.1016/j.cplett.2012.05.044.